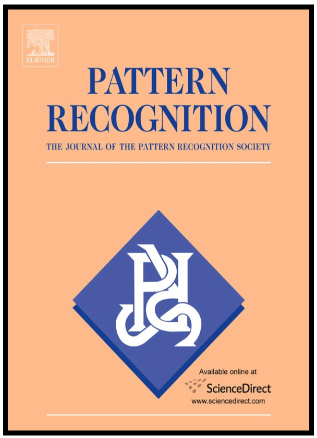

www.elsevier.com/locate/pr

Nonlinear Feature Transformation and Deep Fusion for Alzheimer's Disease Staging Analysis

Bibo Shi, Yani Chen, Pin Zhang, Charles D. Smith, Jundong Liu

PII: S0031-3203(16)30291-6
DOI: http://dx.doi.org/10.1016/j.patcog.2016.09.032
Reference: PR5894

To appear in: *Pattern Recognition*

Received date: 1 February 2016
Revised date: 17 September 2016
Accepted date: 21 September 2016

Cite this article as: Bibo Shi, Yani Chen, Pin Zhang, Charles D. Smith anc Jundong Liu, Nonlinear Feature Transformation and Deep Fusion for Alzheimer' Disease Staging Analysis, *Pattern Recognitior* http://dx.doi.org/10.1016/j.patcog.2016.09.032

Nonlinear Feature Transformation and Deep Fusion for Alzheimer's Disease Staging Analysis

Bibo Shi[a], Yani Chen[b], Pin Zhang[b], Charles D. Smith[c], Jundong Liu[b,*],
For the Alzheimer's Disease Neuroimaging Initiative[**]

[a]*Duke University Medical Center*
Department of Radiology
Duke University, Durham NC 27710
[b]*School of Electrical Engineering and Computer Science*
Ohio University, Athens OH 45703
[c]*Department of Neurology*
University of Kentucky, Lexington KY 40503

Abstract

In this study, we develop a novel nonlinear metric learning method to improve biomarker identification for Alzheimer's Disease (AD) and Mild Cognitive Impairment (MCI). Formulated under a constrained optimization framework, the proposed method learns a smooth nonlinear feature space transformation that makes the mapped data more linearly separable for SVMs. The thin-plate spline (TPS) is chosen as the geometric model due to its remarkable versatility and representation power in generating sophisticated yet smooth deformations. In addition, a deep network based feature fusion strategy through stacked denoising sparse auto-encoder (DSAE) is adopted to integrate cross-sectional and longitudinal features estimated from MR brain images. Using the ADNI dataset, we evaluate the effectiveness of the proposed feature transformation and feature fusion strategies and demonstrate the improvements over the state-of-the-art solutions within the same category.

[*] Corresponding author. Email: liuj1@ohio.edu

[**] Data used in preparation of this article were obtained from the Alzheimers Disease Neuroimaging Initiative (ADNI) database (`adni.loni.usc.edu`). As such, the investigators within the ADNI contributed to the design and implementation of ADNI and/or provided data but did not participate in analysis or writing of this report. A complete listing of ADNI investigators can be found at: `http://adni.loni.usc.edu/wp-content/uploads/how_to_apply/ADNI_Acknowledgement_List.pdf`

Keywords: Metric Learning, Alzheimer's Disease (AD), Mild Cognitive Impairment (MCI), SVM classifier, Feature Fusion, Deep Neural Networks

1. Introduction

Alzheimer's Disease (AD), the most common form of dementia, affects more than five million Americans in 2015 [1]. AD is characterized by rapid forgetting, disorientation in time, and wayfinding difficulties severe enough to impair day to day activities. While the cause and mechanism of AD are still not well understood, it is commonly believed that the pathophysiologic process of AD takes place years or even decades before clinical symptoms develop. Individuals with amnestic Mild Cognitive Impairment (MCI) condition have been shown to have a high likelihood of progression to AD, with an annual conversion rate of $5-10\%$ [2].

As no evidence yet suggests that the pathophysiologic progression in AD can be reversed, it is of great importance to make accurate diagnosis and initiate treatments at the earliest stages of AD, including MCI and presymptomatic states.

Identification and validation of biological markers (biomarkers) for AD/MCI are crucial in this pursuit. β-amyloid, total tau and phospho-tau-181 in cerebrospinal fluid (CSF) are three well-accepted CSF biomarkers of neurodegeneration helpful for AD diagnosis. Neurodegeneration biomarkers, such as atrophy in hippocampi, can also predict further cognitive declines in MCI [3]. Neuroimaging modalities, including Magnetic Resonance Imaging (MRI) and Positron Emission Tomography (PET), provide non-invasive approaches to measure the accepted biomarkers, as well as search for new biomarkers in CSF and brain structures.

The Alzheimer's Disease Neuroimaging Initiative (ADNI) [4] has provided a wealth of new data including structural and functional MR images to support the research on intervention, prevention and treatments of AD. Significant research efforts have been conducted using ADNI data to identify neuroimage biomarkers for the diagnoses of AD/MCI and various mixed pathologies. Machine learning techniques are widely employed, and there is a pressing need to refine the solutions of feature extraction, transformation and fusion to achieve more accurate patient classification.

Metric functions are a pivotal component of distance-based machine learning solutions, e.g., k-NN and k-means. Many pattern classification algorithms rely on the Euclidean metric to compute pairwise dissimilarities, which assigns an equal weight to each feature component. Replacing the Euclidean with a metric learned from the inputs can often improve the algorithm's performance significantly [5, 6]. Learning such a metric is equivalent to learning a feature transformation [5]. Depending on the transformation to be sought, metric learning (ML) can be divided into linear and nonlinear groups [6]. Linear models [7, 8, 9, 10, 11, 12] commonly attempt to estimate a "best" affine transformation to deform the feature space, such that the resulted pairwise Mahalanobis distances would well agree with the supervisory information brought by training samples. While easy to use and convenient to optimize, linear models possess limited expressive power and separation capability in handling data with nonlinear structures. Nonlinear models [13, 14, 15, 16, 17, 18, 19, 20] are usually designed through kernelization or localization of certain linear models. The idea of localization is to build an overall nonlinear metric through combination of multiple piecewise linear metrics that are learned based on either local neighborhoods or class memberships. Although the multi-metric strategies are commonly more powerful in accommodating nonlinear structures, generalizing these methods to fit other classifiers than k-NN is not trivial. To avoid nonsymmetric metrics, extra cares are often needed to ensure the smoothness of the transformed feature space.

Feature extraction and fusion from the ADNI database is also in great need of further exploration. In neuroimaging applications, features are commonly sought at three levels: voxel, patch and regions of interest (ROI). For structural features extracted from brain MRIs, cortical thickness [21], volumetry of brain structures [22, 23] and voxel tissue probability maps [24, 25] across the whole brain or around certain ROIs, are among the popular choices. Patch-based solutions [25, 26, 27], first dividing the original image into small-sized patches and then extracting their feature vectors, have gained great popularity in recent years. Patch extraction is relatively easy to carry out, as it does not require ROI identification or image segmentation. Comparing with voxel features, patch features can still very well capture subtle brain changes, but with greatly reduced dimensionalities. While impressive classification results have been reported, most studies use either cross-sectional features obtained at one point in time [28, 29, 25, 27, 30, 31, 32], or “static” longitudinal volumetric information acquired at two or multiple time points but only through structural segmentation [33, 34, 35]. In part due to the unavailability of deformation data in ADNI, “dynamic” longitudinal information such as the atrophies at various gray matter (GM) areas, which is a major hallmark in the progression of AD, has not been fully utilized in the literature.

Deep learning models, which have recently revolutionized many domains of artificial intelligence (AI) including image search and speech recognition, may provide a set of successful methods to enhance fusion of multi-modality neuroimaging data, allowing improved clinical reliability in AD/MCI diagnoses [36, 25]. The main promise of deep learning is replacing handcrafted features with multiple levels of representations of the data, obtained via (unsupervised) learning. These representations, each corresponding to a level of abstraction, form a hierarchy of concepts. Inspired by these significant developments in AI, we exploit deep neural networks in our study to build a feature fusion architecture to incorporate cross-sectional and longitudinal information.

1.1. Contributions and paper overview

In this paper, we propose to improve the quality of AD/MCI neuroimage biomarker identification along two directions: 1) feature space transformation through a novel nonlinear metric learning (ML) technique, and 2) extraction and integration of dynamic longitudinal atrophy features into the classification framework. The proposed ML solution is a generalization of linear ML through the application of a deformable geometric model — the thin-plate spline (TPS) - to transform the feature space in SVMs. Toward the integration of longitudinal information, we explore different choices, and adopt a deep neural network model – multi-modal stacked denoising sparse auto-encoder (MM-S-DSAE), to fuse cross-sectional (baseline) and longitudinal atrophy (yearly change at baseline features extracted from MR brain images.

The remaining sections of this paper are organized as follows: We start with the presentation of our TPS-SVM solution in section 2. Then, in section 3, we describe the data and features used in our experiments for AD/MCI diagnosis, where TPS-SVM is employed as the final classifier. In section 4, we present the experimental results and evaluate the performance of individual components and the overall pipeline. Finally, we conclude this paper with more discussions and future directions in section 5.

2. Thin-Plate Spline (TPS) Based Nonlinear Feature Transformation

Most of the existing ML solutions rely on pairwise distances among training data points to seek optimal feature transformations, and therefore they are best suited to improve nearest neighbor (NN) based algorithms, such as k-NN and k-means. Typically, metric learning algorithms are utilized as a preprocessing step, followed by the application of the learned metric or transformation to the ensuing classification or clustering algorithms. However, it has been empirically demonstrated in [37] that such “feature-transform-then-classification” strategy does not always improve the performance of the ensuing classifiers, especially those that are non-NN based. In recent years, ML has been applied to SVM models [37, 38]. To date, however, the existing SVM-based ML models employ only linear transformations, limiting their capabilities in dealing with complex data.

The nonlinear feature transformation solution proposed in this study is a direct generalization of linear metric learning through the application of deformable geometric models to transform the entire feature space. We choose the thin-plate splines (TPS) as the transformation model, as TPS are well-known for their remarkable versatility and representation power in accounting for high-order deformations. The nonlinear feature transformation and the SVM classifier are simultaneously optimized through an efficient EM-like (expectation-maximization) algorithm. To the best of our knowledge, this is the first work that utilizes nonlinear dense transformations, or spatially varying deformation models in metric learning, with a specific design for SVMs. In the coming paragraphs, we will describe the theoretical background of the TPS under the general context of geometric transformations, then present our proposed *TPS Metric Learning for Support Vector Machines* (TML-SVM) model.

2.1. TPS transformation

When utilized to align a set of n corresponding point-pairs $\mathbf{u}_i$ and $\mathbf{v}_i$, ($i = 1, \dots, n$), a TPS transformation is a mapping function $f(\mathbf{x}) : \mathbb{R}^d \to \mathbb{R}^d$ within a suitable Hilbert space $\mathcal{H}$, that simultaneously matches $\mathbf{u}_i$ and $\mathbf{v}_i$ and minimizes the following TPS smoothness penalty functional:

$$J_m^d(f) = \int ||\mathcal{D}^m f||^2 \mathrm{d}X = \sum_{a_1+\cdots+a_d=m} \frac{m!}{a_1!\dots a_d!} \int\dots\int \left(\frac{\partial^m f}{\partial x_1^{a_1}\dots\partial x_d^{a_d}}\right)^2 \prod_{j=1}^{d} \mathrm{d}x_j, \tag{1}$$

where $\mathcal{D}^m f$ is the matrix of m-th [1] order partial derivatives of $f(\cdot)$, with a_k ($k = 1, 2, ..., d$) being positive. $\mathrm{d}X = \prod_{j=1}^{d} \mathrm{d}x_j$, and x_j are the components of $\mathbf{x}$. The classic solution of Eqn. (1) has a representation in terms of a radial basis function (TPS interpolation function),

$$f_k(\mathbf{x}) = \sum_{i=1}^{n} \psi_i G(||\mathbf{x} - \mathbf{x}_i||) + \boldsymbol{\ell}^T \mathbf{x} + c, \qquad (k = 1, 2, ..., d) \tag{2}$$

where f_k is the kth vector component of $f(\cdot)$, $||.||$ denotes the Euclidean norm and $\{\psi_i\}$ ($i = 1, 2, ..., n$) are a set of weights for the nonlinear part. $\boldsymbol{\ell}$ and c

[1] m is a positive integer. In order to bound the mapping function $f(\cdot)$ within a reproducing kernel Hilbert space endowed with the seminorm $J_m^d(f)$, it is necessary and sufficient that $2m - d > 0$. Please refer to [39] for more details and proof.

are the weights for the linear part. The corresponding radial distance kernel of TPS, which is the Green's function to solve Eqn. (1), is as follows:

$$G(\mathbf{x}, \mathbf{x}_i) = G(||\mathbf{x} - \mathbf{x}_i||) \propto \begin{cases} ||\mathbf{x} - \mathbf{x}_i||^{2m-d} \ln ||\mathbf{x} - \mathbf{x}_i||, & \text{if } 2m - d \text{ is even;} \\ ||\mathbf{x} - \mathbf{x}_i||^{2m-d}, & \text{otherwise.} \end{cases} \tag{3}$$

For more details about TPS, we refer readers to [40, 39].

The TPS transformation for point interpolation, as specified in Eqn. (2), can be employed as the geometric model to deform the input space for nonlinear metric learning. Such a transformation would ensure certain desired smoothness as it minimizes the bending energy $J_m^d(f)$ in Eqn. (1). Within the metric learning setting, let $\mathbf{x}$ be one of the training samples in the original feature space $\mathcal{X}$ of d dimensions, and $f(\mathbf{x})$ be the transformed destination of $\mathbf{x}$, also of d dimensions. Through a straightforward mathematical manipulations [41], we can get $f(\mathbf{x})$ in matrix format:

$$f(\mathbf{x}) = L\mathbf{x} + \Psi \begin{pmatrix} G(\mathbf{x}, \mathbf{x}_1) \\ \cdots \\ G(\mathbf{x}, \mathbf{x}_p) \end{pmatrix} = L\mathbf{x} + \Psi \vec{G}(\mathbf{x}), \tag{4}$$

where L (size $d \times d$) is a linear transformation matrix, Ψ (size $d \times p$) is the weight matrix for the nonlinear parts, and p is the number of anchor points $(\mathbf{x}_1, \ldots, \mathbf{x}_p)$ to compute the TPS kernel. We can use all the training data points as the anchor points. However, in practice, p anchor points are extracted through k-medoids method [42, 43] under the consideration of reducing computational cost.

2.2. TML-SVM

The standard SVMs simultaneously minimize the empirical classification error and maximize the geometric margin. In the context of metric learning, the feature space is transformed and therefore additional constraints need to be imposed to ensure the notion of *maximum margin* remains meaningful. To this end, we adopt the *Margin-Radius-Ratio* bounded paradigm [44, 38] as such an enforcer, as described below.

Given training dataset $\mathcal{X} = \{\mathbf{x}_i |\ \mathbf{x}_i \in \mathbb{R}^d, i = 1, \cdots, n\}$ together with the class label information $y_i \in \{-1, +1\}$, our proposed TML-SVM jointly learns a nonlinear transformation $f(\cdot)$ and a SVM classifier:

$$\begin{aligned} \min_{L,\Psi,\mathbf{w},b} \quad & J = \frac{1}{2}\|\mathbf{w}\|^2 + C_1 \sum_{i=1}^{n} \xi_i + C_2 \|\Psi\|_F^2 \\ \text{s.t.} \quad & y_i(\mathbf{w}^T f(\mathbf{x}_i) + b) \geq 1 - \xi_i, \quad \xi_i \geq 0, \quad \forall i = 1 \ldots n;\ (\text{I \& II}) \\ & \|f(\mathbf{x}_i) - \mathbf{x}_c\|^2 \leq 1, \quad \forall i = 1 \ldots n;\ (\text{III}) \\ & \sum_{i=1}^{p} \Psi_i^k = 0, \quad \sum_{i=1}^{p} \Psi_i^k \mathbf{x}_i^k = 0,\ \forall k = 1 \ldots d.\ (\text{IV}) \end{aligned} \tag{5}$$

$f(\cdot)$ is in the form of Eqn. (4), Ψ^k is the kth column of Ψ, and $\mathbf{x}^k$ is the kth component of $\mathbf{x}$. In addition to the components for the traditional soft margin SVMs, another component $\|\Psi\|_F^2$, the squared Frobenius norm of Ψ, is added to the objective function as a regularizer to prevent overfitting. C_1 and C_2 are two trade-off hyper-parameters. The first two nonequivalent constraints (I and II) are the same as used in traditional SVMs. The third nonequivalent term (III) is a unit-enclosing-ball constraint from the *Margin-Radius-Ratio* paradigm, which forces the radius of minimum-enclosing-ball to be unit in the transformed space and avoids trivial solutions. $\mathbf{x}_c$ is the center of all samples. The last two equivalent constraints (IV) are used to maintain the properties for TPS transformation at infinity.

To solve this optimization problem, we propose an efficient EM-like iterative minimization algorithm by updating $\{\mathbf{w}, b\}$ and $\{L, \Psi\}$ alternatingly. Firstly, we centralize the input data: $\mathbf{x}_i \leftarrow \mathbf{x}_i - \frac{1}{n}\sum_{i=1}^{n} \mathbf{x}_i$, so the unit-enclosing-ball constraint can be simplified to $\|f(\mathbf{x}_i)\|^2 \leq 1$.

With $\{L, \Psi\}$ fixed, $f(\mathbf{x}_i)$ is explicit, and Eqn. (5) can be reformulated as:

$$\begin{aligned} \min_{\mathbf{w},b} \quad & J = \frac{1}{2}\|\mathbf{w}\|_2^2 + C_1 \sum_{i=1}^{n} \xi_i \\ \text{s.t.} \quad & y_i(\mathbf{w}^T f(\mathbf{x}_i) + b) \geq 1 - \xi_i, \quad \xi_i \geq 0, \quad \forall i = 1 \ldots n. \end{aligned} \tag{6}$$

This becomes exactly the primal form of soft margin SVMs, which can be solved by off-the-shelf SVM solvers.

With $\{\mathbf{w}, b\}$ fixed, Eqn. (5) can be reformulated as:

$$\begin{aligned}
\min_{L,\Psi} \quad & J = C_1 \sum_{i=1}^{n} \xi_i + C_2 \|\Psi\|_F^2 \\
\text{s.t.} \quad & y_i(\mathbf{w}^T f(\mathbf{x}_i) + b) \geq 1 - \xi_i, \quad \xi_i \geq 0, \quad \forall i = 1 \ldots n; \\
& \|f(\mathbf{x}_i)\|^2 \leq 1, \quad \forall i = 1 \ldots n; \\
& \sum_{i=1}^{p} \Psi_i^k = 0, \quad \sum_{i=1}^{p} \Psi_i^k \mathbf{x}_i^k = 0, \ \forall k = 1 \ldots d.
\end{aligned} \tag{7}$$

By using hinge loss function, we can eliminate variables ξ_i, and reformulate Eqn. (7) as:

$$\begin{aligned}
\min_{L,\Psi} \quad & J = C_1 \sum_{i=1}^{n} \max[0, 1 - y_i(\mathbf{w}^T f(\mathbf{x}_i) + b)]^2 + C_2 \|\Psi\|_F^2 \\
\text{s.t.} \quad & \|f(\mathbf{x}_i)\|^2 \leq 1, \quad \forall i = 1 \ldots n; \\
& \sum_{i=1}^{p} \Psi_i^k = 0, \quad \sum_{i=1}^{p} \Psi_i^k \mathbf{x}_i^k = 0, \ \forall k = 1 \ldots d.
\end{aligned} \tag{8}$$

As the squared hinge loss function is differentiable, it is not difficult to differentiate the objective function w.r.t. L and Ψ. Thus, we can use a gradient based optimizer to get a local minimum for Eqn. (8), with the gradient computed as:

$$\begin{aligned}
\frac{\partial J}{\partial \Psi} &= -2C_1 \sum_{i=1}^{n} \max[0, 1 - y_i(\mathbf{w}^T f(\mathbf{x}_i) + b)](y_i \mathbf{w} \vec{G}^T(\mathbf{x}_i)) + 2C_2 \Psi \\
\frac{\partial J}{\partial L} &= -2C_1 \sum_{i=1}^{n} \max[0, 1 - y_i(\mathbf{w}^T f(\mathbf{x}_i) + b)](y_i \mathbf{w} \mathbf{x}_i^T)
\end{aligned} \tag{9}$$

To sum it up, the optimal nonlinear transformation defined by $\{L, \Psi\}$ along with the optimal SVM classifier coefficients $\{\mathbf{w}, b\}$ can be obtained by an EM-like iterative procedure, as described in Algorithm 1.

The algorithm is initialized with an identity matrix for L, a zero matrix for $\mathbf{\Psi}$, and two step tolerances $\epsilon_{\mathbf{w}+b}$ and $\epsilon_{L+\mathbf{\Psi}}$ for TPS and SVM parameters, respectively. After each iteration, we check the updates of the TPS parameters,

[1] We use a SQP based constrained optimizer "fmincon" in Matlab Optimization Toolbox to solve Eqn. (8). In practice, the convergence for the second inner step is not necessary, so we use an early stop strategy to speed up the whole algorithm.

Algorithm 1 TPS Metric Learning for SVMs (TML-SVM)

```
**Input:** training dataset $\mathcal{X} = \{\mathbf{x}_i |\ \mathbf{x}_i \in \mathbb{R}^d, i = 1, \cdots, n\}$,
        class label information $y_i \in \{-1, +1\}$
**Initialize:** $\Psi = \mathbf{0}$, $L = \mathbf{I}$
.....................................................................
**Centralize the input data:** $\mathbf{x}_i \leftarrow \mathbf{x}_i - \frac{1}{n}\sum_{i=1}^{n} \mathbf{x}_i$
**Iterate the following two steps:**
  **(1) Update** $\{\mathbf{w}, b\}$ **with fixed** $\{L, \Psi\}$ **:**
        Compute the transformed data $f(\mathbf{x}_i)$ by following Eqn. (4)
        Update $\{\mathbf{w}, b\}$ by using off-the-shelf SVM solver with input of $f(\mathbf{x}_i)$
  **(2) Update** $\{L, \Psi\}$ **with fixed** $\{\mathbf{w}, b\}$ **:**
        Update $\{L, \Psi\}$ by solving Eqn. (8) through gradient based optimizers
1
 **until convergence**
.....................................................................
**Output:** the optimal SVM classifier defined by $\{\mathbf{w}, b\}$,
        the nonlinear TPS transformation defined by $\{L, \Psi\}$
```

L and $\mathbf{\Psi}$, from the previous iteration. If the norms of both changes are smaller than $\epsilon_{L+\mathbf{\Psi}}$, the algorithm is terminated. Otherwise, we check the step updates for $\mathbf{w}$ and b. If their magnitudes are smaller than $\epsilon_{\mathbf{w}+b}$, we terminate the algorithm. Meanwhile, we also set a maximum iteration count N_{max} to control the stopping of the optimization.

3. Neuroimage Data and Features

3.1. ADNI data

The neuroimage data used in this work were obtained from the ADNI database [4]. We consider only the subjects for whom the baseline (M0) visits and 12-month follow-up (M12) T1-weighted MRIs, together with their *MIDAS Whole Brain Masks*, are all available. As a result, 338 subjects were selected: 94 patients with AD, 121 with MCI and 123 normal controls (NC). More detailed information, including the demographics and clinical evaluations of the subjects, i.e., Mini Mental State Examination (MMSE) and Clinical Dementia Rating (CDR) scores, of the studied subjects at their baseline visits, are shown in Table 1.

Table 1: Demographic and clinical information of the studied subjects at the baseline.

Diagnosis	Number	Gender (M/F)	Age (mean±sdv.) [min-max]	MMSE (mean±sdv.) [min-max]	CDR (mean±sdv.) [min-max]
AD	94	47/47	75.85 ± 7.2 $[55 - 90]$	23.21 ± 1.9 $[20 - 26]$	0.8 ± 0.25 $[0.5 - 1]$
MCI	121	69/52	75.73 ± 7.8 $[55 - 90]$	26.57 ± 1.7 $[23 - 30]$	0.5 ± 0 $[0.5 - 0.5]$
NC	123	65/58	76.08 ± 5.2 $[62 - 90]$	29.15 ± 0.9 $[26 - 30]$	0 ± 0 $[0 - 0]$

3.2. Feature extraction

In this study, we utilize three types of features, based on 1) gray matter (GM) patches extracted from T1-weighted baseline MP-RAGE MR images; 2) 12-month deformation magnitude (DM) patches estimated through baseline and

12-month follow-up MP-RAGE MRIs; and 3) volumes of 113 cortical and subcortical structures extracted from baseline *FreeSurfer Cross-Sectional Processing aparc+aseg* segmentations ("Aseg" features). Both MP-RAGE and baseline aparc+aseg segmentation data are available under ADNI. The pipeline of our proposed feature extraction framework is illustrated in Fig. 1.

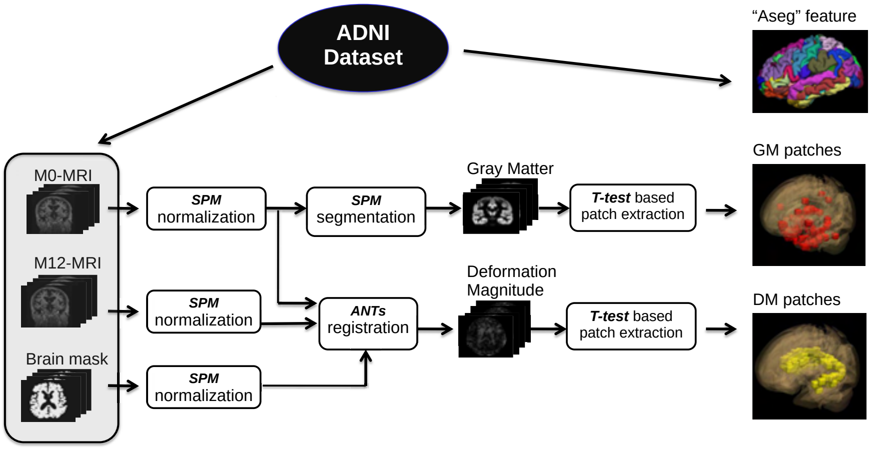

Figure 1: The pipeline of the proposed feature extraction framework.

3.2.1. "GM/DM" features

Recently, patch-level neuroimage features extraction and fusion [27, 25] have been used in producing excellent performance for AD/MCI/NC classifications. The features utilized in their work [27, 25] are cross-sectional, extracted from the baseline MRIs and Positron Emission Tomography images (PETs). In this study, we adopt a similar patch extraction strategy as in [27] to extract two types of patches from the MP-RAGE scans: GM and DM patches. GM patches contain candidate areas where two groups (e.g., AD vs. NC) differ greatly in terms of gray matter densities. DM patches capture the areas where group atrophy patterns are significantly different.

To facilitate the ensuing patch-level operations, the T1-weighted MRIs (at both M0 and M12) were first normalized onto an International Consortium for Brain Mapping template through Statistical Parametric Mapping [45], with the dimensions reduced to $79 \times 79 \times 95$ and the voxel sizes to $2 \times 2 \times 2\ mm^3$. After spatial normalization, each baseline M0-MRI was segmented into three brain tissues: GM, WM and CSF. As GM is more related to AD and MCI pathologies than WM and CSF [25], we choose the GM tissue densities from the baseline MRIs as the cross-sectional information source in our work. A voxel-wise t-test was performed for group comparisons of AD vs. NC and MCI vs. NC. Voxels with statistically significant group difference (with the p-value smaller than 0.05) were identified as the seeds for patch extraction. The mean p-values in the seed voxels' enclosing patches of size $5 \times 5 \times 5$ were then used to sort the patch seeds. Based on their ascending order, we selected the first 100 class-discriminative patches in a greedy manner with the condition that no candidate patch pair should have more than 50% overlapping volume. The average GM densities in these patches form our cross-sectional feature vector, which we call "GM" feature. Fig. 2 is a visualization of the top 20 GM patches that are selected from AD vs. NC and MCI vs. NC group comparisons, respectively.

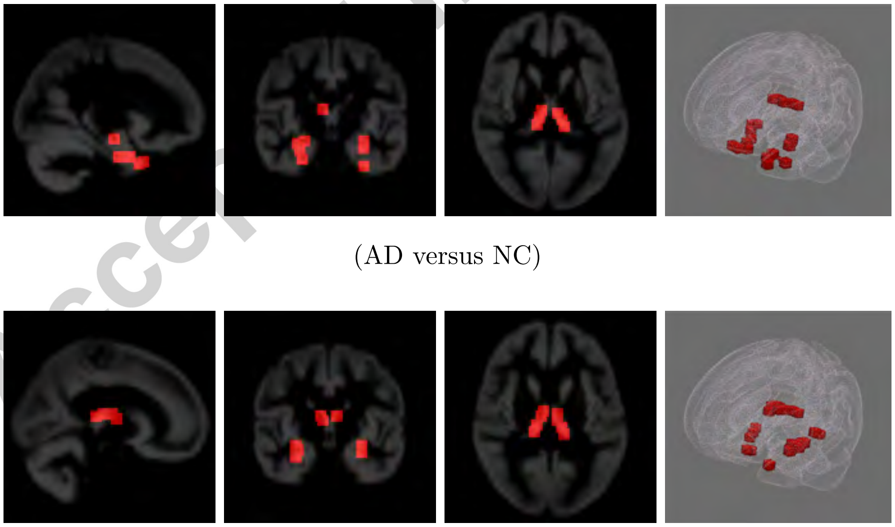

(AD versus NC)

(MCI versus NC)

Figure 2: The top 20 ranked GM patches selected in AD vs. NC and MCI vs. NC group comparisons. The columns from left to right are sagittal, coronal, axial and 3D views.

Our longitudinal DM patches were obtained based on the estimated voxel deformations matching the baseline and follow-up MRIs for each subject. A diffeomorphic registration method provided via ANTs package [46] was utilized to generate the deformation vector fields. To minimize the effect of the soft-tissue shifts outside the brains, a dilated *MIDAS Whole Brain Mask* for each subject was used to specify the registration area for ANTs. We then calculated the magnitude (or length) of the deformation vector at each voxel, and a 3D scalar field of deformation magnitudes (DM) was obtained. Based on the DM scalar fields, we conducted the same group comparison and patch extraction procedure as for the "GM" features. A set of (top 100 ranked) 3D local patches were obtained. The average DM values within these patches form our longitudinal "DM" feature vector. Fig. 3 shows the top 20 DM patches selected from AD vs. NC and MCI vs. NC group comparisons, respectively.

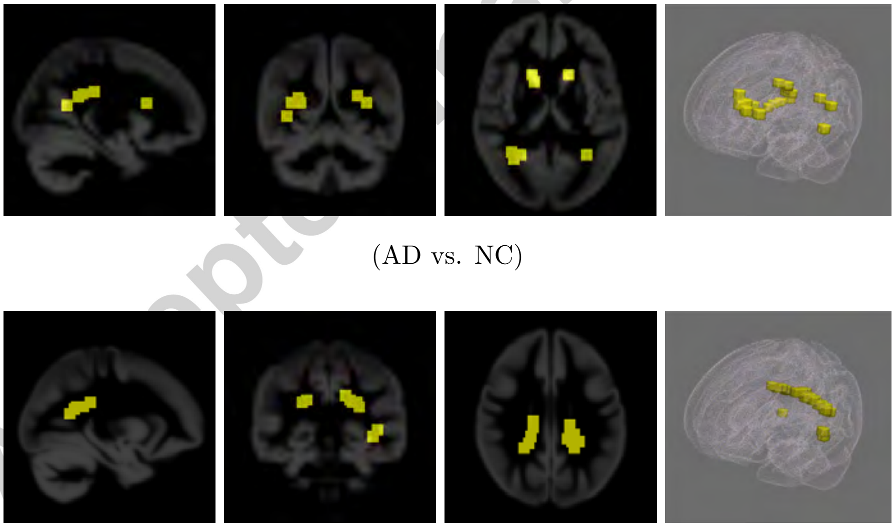

(AD vs. NC)

(MCI vs. NC)

Figure 3: The top 20 ranked DM patches selected in AD vs. NC and MCI vs. NC group comparisons. The columns from left to right are sagittal, coronal, axial and 3D views.

3.2.2. "Aseg" features

Our "GM" and "DM" features are patch-based. To supplement them with ROI information, we also include the volumes of brain structures extractable from *FreeSurfer Cross-Sectional Processing aparc+aseg* segmentation files, available under ADNI. The aparc+aseg segmentation files were extracted from MP-RAGE scans using FreeSurfer [47]. Subcortical structures extracted in aparc+aseg segmentation [48] include left/right hippocampi, left/right caudate, etc., and cortical ROI include precuneus, cuneus, etc. Within the FreeSurfer processing pipeline, all volumetric measurements have been normalized for head size via dividing by the intracranial volume (ICV). This allows for unbiased comparisons between groups at a single time point. In this study, we use 113 volumes at the baseline visits as another set of features for each subject, which we call "Aseg" features. The names of the brain structures generated by FreeSurfer aparc+aseg segmentation can be found in each subjects stats/aseg.stats and stats/aparc.stats files, as described in `https://surfer.nmr.mgh.harvard.edu/fswiki/FsTutorial/AnatomicalROI`. The name list is also included in Appendix A of this paper. For more information regarding ADNI MRI data analysis, including FreeSurfer processing, we refer readers to the data hosting site `http://adni.loni.usc.edu/methods/mri-analysis/`.

3.3. Feature fusion

The feature extraction steps described above produce 100 features from GM and DM patches, respectively, and 113 "Aseg" features from "aparc+aseg" segmentation. Inevitably, there should be redundant or irrelevant features in this set, and the feature dimension, 313, is relatively high for efficient computation. To approach this high dimensionality problem, the three different types of features should be fused with a reduced dimensionality; deep neural network-based models provide a potentially powerful solution. Deep neural networks have been utilized in several recent AD/MCI works [23, 30, 27, 49], with the same goal of learning a latent and compressed representation of the input feature vectors. Stacked auto-encoder [23, 30], restricted Boltzmann machine [27] and convolutional networks [49] are among the choices that have been examined. In this paper, we adopt a different model — stacked denoising sparse auto-encoder (stacked DSAE), which is a combination of denoising and sparse auto-encoders [50, 51]. The "GM/DM/Aseg" features go through stacked DSAE separately, then we utilize another fusion layer on top to further combine the separate outputs. Our approach is different from some recent methods [23, 30]: not only does it maximize the mutual information from different sources, it also enables users to control the size of the fused features, desirable for the goal of dimension reduction.

3.3.1. Stacked denoising sparse auto-encoder (Stacked-DSAE)

The goal of an auto-encoder (AE) is to learn a latent representation for the input vector $\mathbf{x}$ through estimating a nonlinear approximation function $h_{\mathbf{W},\mathbf{b}}(\mathbf{x}) \approx \mathbf{x}$. In order to discover interesting structures from the input, certain type of constraint or regularization needs to be imposed into the network. Sparse auto-encoder learns sparse over-complete representation by ensuring the majority of the hidden nodes "inactive" most of the time. This can be done by adding a sparse penalty into the objective function. Denoising auto-encoder, on the other hand, obtains a more robust representation by cleaning partially corrupted input (denoising). In this work, we combine these two models to construct a denoising sparse auto-encoder (DSAE), and use it as the solution for feature extraction. This choice is based on the nature of the "GM/DM" features. While easy to obtain, the "GM/DM" feature vectors contain many non-discriminative components. DSAE is designed under the hypothesis that it can learn a compressed representation from the rather noisy input.

To build a deep network, we stack multiple DSAEs, wiring the outputs of each hidden layer to the inputs of the successive layer, to form a stacked DSAE. Such multi-layer networks can be pretrained level by level in a greedy fashion. Compared with single layer shallow networks, stacked deep networks are more effective in finding highly nonlinear and complex patterns in data [51]. In this work, we use three separate stacked DSAEs, for "GM", "DM", and "Aseg" features respectively, to extract their latent representations. Similar to the approach in [27], three hidden layers are used in each stacked DSAE, with the parameters decided through grid search. More details regarding the parameter selection will be given in the experimental results section.

3.3.2. Feature fusion through multi-modal stacked DSAE (MM-S-DSAE)

With the latent high level representation discovered by the three stacked DSAEs for "GM/DM/Aseg" features, the next task is to fuse them without losing useful information. Ideally, the output dimension should be further decreased after the integration, leading to a more compact yet still discriminative final feature set. Several strategies are available, as shown in Fig. 4. Black and white circles in this figure represent two different feature types, e.g., "GM" and "DM", and gray circles denote the features after fusion. Fig. 4.(b)∼(d) illustrate three fusion solutions: (b) shows the most intuitive way that concatenates different types of feature in the input layer, and learns a single deep neural network, as used in [23]; (c) learns separate deep neural networks for each feature type, and concatenates the output layers; (d) adds one more fully connected fusion layer on top of (c). In this paper, we choose the last strategy, the so-called multi-modal stacked DSAE (MM-S-DSAE) as the solution to combine "GM", "DM" and "Aseg" features. The advantage of MM-S-DSAE over the other two alternatives has been empirically validated and will be presented in section 4.3.

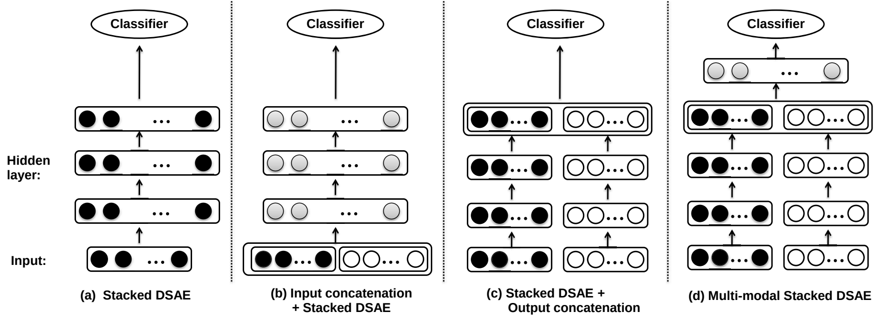
Classifier
Classifier
Classifier
Classifier
Hidden layer:
Input:
(a) Stacked DSAE
(b) Input concatenation + Stacked DSAE
(c) Stacked DSAE + Output concatenation
(d) Multi-modal Stacked DSAE

Figure 4: Deep network structures of stacked DSAE (a), and three fusion strategies (b-d).

4. Experiments and Results

In this section, we evaluate the proposed TML-SVM metric learning and MM-S-DSAE feature fusion models through two binary classification problems: AD vs. NC, and MCI vs. NC. Several experimental setups, including evaluation measures, data partition scheme and the determination of the structure of our MM-S-DSAE, are explained in section 4.1. We present in section 4.2 the experiments to analyze and compare the discriminative power of individual feature types and their combinations. In section 4.3, MM-S-DSAE will be evaluated against other feature fusion strategies. Improvements made by TML-SVM over other classifiers will be examined in section 4.4. Finally, we compare our method with some recently reported solutions that also use ADNI database for AD/MCI diagnosis.

4.1. Experimental setups

4.1.1. Performance measures and data partition

Various classification solutions are compared in this section and their performance is measured with three evaluation metrics: classification accuracy (ACC), i.e., the proportion of correctly classified subjects among the whole test set; sensitivity (SEN), i.e., the proportion of correctly classified AD (or MCI) patients; and specificity (SPE), i.e., the proportion of correctly classified normal controls. In addition to *means* and *standard deviations*, we also report the p-values from the paired t-test when comparing each performance measure of two different methods. To ensure a good generalizability for each experiment and comparison, we run every experiment 10 times with different random 5-fold splits: three folds for training, one fold for validation of hyper-parameters, and one fold for testing.

4.1.2. Determination of the structure of MM-S-DSAE

The topology of MM-S-DSAE is illustrated in Fig. 4.(d). We use three hidden layers for the underlying stacked DSAE. The numbers of the three layers' hidden nodes are selected from $[100, 300, 500, 1000] - [50, 100] - [10, 20, 30]$ (bottom to up). The hyper-parameters for sparsity control and denoising corruption are both set to 0.2. For the top fusion layer in MM-S-DSAE, the number of hidden nodes is selected from $[3, 5, 8, 10, 15, 20]$. The optimal number of hidden nodes for each layer is determined by the classification performance (accuracy) of the softmax regression classifier with grid search, similar to [23].

4.1.3. Choice of classifiers

We use softmax regression model in our experiments, with the following considerations. Being regarded as "the classifier for stacked auto-encoder" [23], softmax is utilized as the "intuitive" classifier to reduce the potential bias introduced by any particular classifier, which is ideal for comparing the performance of different features or different fusion strategies. Using softmax as the classifier also makes "fine-tuning" of stacked DSAE and MM-S-DSAE straightforward. Due to its popularity, we include softmax as one of the competing algorithms to evaluate our TML-SVM classifier in section 4.4.

4.2. Comparisons of different features

The first set of experiments is to investigate the efficacy of different features in distinguishing AD and MCI from normal controls. Specifically, five types of features, including the aforementioned "GM", "DM", "Aseg" features, and two different combinations of them, i.e, "GM & Aseg" – the combination of two static cross-sectional features at the baseline visit, "GM & DM & Aseg" – the combination of both static cross-sectional and longitudinal atrophy features, are evaluated based on three performance measures, ACC, SEN, and SPE. In addition, to answer the question if the high level representations learned from MM-S-DSAE are indeed more discriminative than the original raw features, we conducted experiments for both "deep" and "raw" versions [2] of the five feature

[2] In Table 2,"XX (raw)" indicates the results are produced with the original raw features, and "XX (deep)" are for the features generated through deep neural networks. We use single modal stacked DSAE to extract "GM (deep)", "DM (deep)", "Aseg (deep)", and MM-S-DSAE to extract "GM & Aseg (deep)", "GM & DM & Aseg (deep)".

types. The overall classification results, averaged over 10 runs, are presented in Table 2.

Table 2: Comparisons of five different features for AD vs. NC and MCI vs. NC classifications. Boldface denotes the best performance for each measure.

AD versus NC					
Classifier	**Features**	**Hidden nodes** [3]	**ACC**(%)	**SEN**(%)	**SPE**(%)
Softmax	GM (raw)	——	77.52 ± 1.91	70.75 ± 3.14	82.67 ± 2.18
	GM (deep)	500-100-10	81.44 ± 0.77	75.21 ± 1.35	86.17 ± 1.14
	DM (raw)	——	70.23 ± 1.29	66.84 ± 1.34	72.85 ± 2.20
	DM (deep)	1000-100-30	79.02 ± 0.93	74.07 ± 0.93	82.83 ± 1.15
	Aseg (raw)	——	83.72 ± 1.32	79.53 ± 2.04	86.92 ± 1.74
	Aseg (deep)	100-50-30	84.85 ± 1.57	80.82 ± 3.35	87.93 ± 2.07
	GM&Aseg (raw)	——	85.21 ± 2.24	80.67 ± 2.46	88.69 ± 2.59
	GM&Aseg (deep)	···-10	86.26 ± 1.53	81.95 ± 2.18	89.56 ± 1.98
	GM&DM&Aseg (raw)	——	87.47 ± 1.11	83.63 ± 1.85	90.41 ± 1.72
	GM&DM&Aseg (deep)	···-8	**88.73 ± 1.04**	**84.86 ± 2.08**	**91.69 ± 1.68**
MCI versus NC					
Classifier	**Features**	**Hidden nodes** [3]	**ACC**(%)	**SEN**(%)	**SPE**(%)
Softmax	GM (raw)	——	52.49 ± 3.41	53.90 ± 4.86	51.14 ± 3.41
	GM (deep)	1000-100-20	75.19 ± 1.36	74.12 ± 2.24	76.31 ± 1.73
	DM (raw)	——	55.57 ± 1.99	59.98 ± 3.94	51.21 ± 1.69
	DM (deep)	300-100-20	69.97 ± 1.03	64.14 ± 2.23	75.73 ± 0.84
	Aseg (raw)	——	53.43 ± 2.33	56.39 ± 2.89	50.48 ± 2.80
	Aseg (deep)	1000-100-20	74.30 ± 1.77	73.70 ± 2.27	74.88 ± 3.08
	GM&Aseg (raw)	——	53.81 ± 2.35	57.02 ± 2.98	50.67 ± 3.59
	GM&Aseg (deep)	···-15	78.47 ± 2.02	76.76 ± 1.99	80.15 ± 3.17
	GM&DM&Aseg (raw)	——	57.10 ± 1.86	58.38 ± 2.47	55.81 ± 2.27
	GM&DM&Aseg (deep)	···-8	**80.91 ± 1.53**	**79.07 ± 2.27**	**82.70 ± 1.35**

From Table 2, it can be observed that the learned "deep" features far outperform the corresponding original "raw" features, especially for the MCI vs. NC classification. The "GM & DM & Aseg" feature is a typical example. The deep version has significantly better performance [4] than the direct concatenation of the original raw features, "GM & DM & Aseg (raw)". More specifically,

[3] For single modal stacked DSAE, we present the optimal number of hidden nodes for each of three hidden layer (bottom to up); for MM-S-DSAE, we only present the optimal number of hidden nodes for the last fusion layer, since the previous layers stay the same as in the single modal ones.

[4] To claim "significantly better" or "significantly improve" in this section, a two-sided *p*-

for AD vs. NC classification, the ACC from "raw" to "deep" has been significantly improved (p-value = 0.017). For MCI vs. NC classification, all three performance measures (ACC, SEN, SPE) are significantly improved (p-values < 0.0001). Furthermore, it is evident that combining longitudinal and baseline features improves classification performance – the fused "GM & DM & Aseg (deep)" feature has the highest ACC, SEN and SPE for both AD vs. NC and MCI vs. NC classifications, with significantly improved performance over the other four feature types also learned from deep networks, "GM (deep)", "DM (deep)", and "Aseg (deep)", and " GM & Aseg (deep)". For example, the second best feature type in Table 2, " GM & Aseg (deep)", the combination of static cross-sectional features at the baseline visit, is significantly outperformed by the "GM & DM & Aseg (deep)" feature for both AD vs. NC (p-values < 0.02) and MCI vs. NC (p-values < 0.04) classifications.

To further illustrate the role of the proposed dynamic longitudinal feature ("DM" feature), we conducted another set of comparative experiments that include static features extracted from 12-month follow-up MRIs, specifically "GM", "Aseg" features at 12-month follow-up visits. Those two features were extracted through a similar pipeline as presented in Section 3, but from the T1-weighted MP-RAGE MR images at 12-month visits, denoted as "GM-12", "Aseg-12". It would be pointless to spend extra efforts to extract dynamic longitudinal information between MRIs at baseline and follow-up visits, if there is no improvement over simply using static cross-sectional features extracted from the follow-up visits. For this purpose, we compared the performance of the following two sets of features, "GM" vs. "GM-12" vs. "GM & DM", and " GM & Aseg" vs. "GM-12 & Aseg-12" vs. "GM & DM & Aseg ". In Table 3, we present the results for those features generated from deep neural networks.

From the results, it can be observed that effort spent on the extraction of dynamic longitudinal information made a significant difference, especially

value of < 0.05 resulted from "two-sample Student's t-test" is the criterion for statistical significance.

for the MCI vs. NC classification where brain anatomical changes in MCI subjects are subtle. Clearly the static features extracted at a later follow-up visit have more discriminative power than the ones extracted from baseline visits, especially for AD vs. NC classification. This can be gleaned from the comparison results of “GM” vs. “GM-12” and “GM & Aseg” vs. “GM-12 & Aseg-12” in Table 3. However, by integrating dynamic longitudinal information into static baseline features, the resulted combination generally outperforms just the static features extracted from follow-up visits for both AD vs. NC, and MCI vs. NC classifications. Specifically, the fused “GM & DM” feature has significantly better ACC and SEN measures than static “GM-12” feature for AD vs. NC classification (p-values < 0.0001) and MCI vs NC classification (p-values < 0.0001). The trend remains after the ROI feature “Aseg” is included. “GM & DM & Aseg” still has the highest ACC, SEN and SPE for both AD vs. NC and MCI vs. NC classifications, with significantly better results in all three measures (ACC, SEN and SPE) than “GM-12 & Aseg-12” for MCI vs. NC classification (p-values < 0.04), and slightly better results for AD vs. NC classification (p-values > 0.05).

Table 3: Comparisons between static and dynamic longitudinal features for AD vs. NC and MCI vs. NC classifications.

AD versus NC

Classifier	**Features**	**Hidden nodes**	**ACC**(%)	**SEN**(%)	**SPE**(%)
Softmax	GM	500-100-10	81.44 ± 0.77	75.21 ± 1.35	86.17 ± 1.14
	GM-12	500-100-20	83.05 ± 0.37	75.97 ± 0.53	**88.48 ± 0.36**
	GM&DM	···-5	**86.92 ± 0.60**	**86.73 ± 1.59**	87.09 ± 0.59
	GM&Aseg	···-10	86.26 ± 1.53	81.95 ± 2.18	89.56 ± 1.98
	GM-12&Aseg-12	···-3	87.63 ± 1.49	84.25 ± 2.28	90.21 ± 2.42
	GM&DM&Aseg	···-8	**88.73 ± 1.04**	**84.86 ± 2.08**	**91.69 ± 1.68**

MCI versus NC

Classifier	**Features**	**Hidden nodes**	**ACC**(%)	**SEN**(%)	**SPE**(%)
Softmax	GM	1000-100-20	75.19 ± 1.36	74.12 ± 2.24	76.31 ± 1.73
	GM-12	500-100-20	75.43 ± 0.60	64.46 ± 0.75	**86.26 ± 0.94**
	GM&DM	···-10	**78.51 ± 1.24**	**78.61 ± 1.73**	78.43 ± 2.39
	GM&Aseg	···-15	78.47 ± 2.02	76.76 ± 1.99	80.15 ± 3.17
	GM-12&Aseg-12	···-3	78.62 ± 1.57	76.63 ± 1.17	80.59 ± 2.59
	GM&DM&Aseg	···-8	**80.91 ± 1.53**	**79.07 ± 2.27**	**82.70 ± 1.35**

4.3. Comparisons of different feature fusion strategies

The second set of experiments is to test the effectiveness of our MM-S-DSAE design in improving AD/MCI vs. NC classifications, with four other feature fusion strategies compared: 1) concatenation of the original three raw features ("GM", "DM", and "Aseg" features); 2) traditional "PCA based" strategy, i.e., concatenate the three raw features, and use Principle Component Analysis (PCA) to reduce the dimension with 99% variances kept; 3) "Input concatenation + Stacked DSAE", as shown in Fig. 4.(b); and 4) "Stacked DSAE + Output concatenation", as shown in Fig. 4.(c). We adopt the same performance measures (ACC, SEN, SPE) and experimental setting (5-fold splits with 10 runs), and use softmax regression classifier as in Section 4.2. The classification results of each strategy for AD/MCI vs. NC are summarized in Table 4.

Table 4: Five feature fusion strategies for AD vs. NC and MCI vs. NC classifications.

AD versus NC

Classifier	**Feature**	**Hidden nodes** [5]	**ACC**(%)	**SEN**(%)	**SPE**(%)
Softmax	Direct concatenation	——	87.47 ± 1.11	83.63 ± 1.85	90.41 ± 1.72
	PCA based	——	86.12 ± 0.97	81.88 ± 2.30	89.34 ± 1.25
	Input concat. + S-DSAE	1000-500-10	87.92 ± 1.50	**86.30 ± 3.24**	89.17 ± 1.28
	S-DSAE + Output concat.	···-70	87.46 ± 1.09	82.54 ± 1.89	91.20 ± 2.17
	MM-S-DSAE	···-8	**88.73 ± 1.04**	84.86 ± 2.08	**91.69 ± 1.68**

MCI versus NC

Classifier	**Feature**	**Hidden nodes**	**ACC**(%)	**SEN**(%)	**SPE**(%)
Softmax	Direct concatenation	——	57.10 ± 1.86	58.38 ± 2.47	55.81 ± 2.27
	PCA based	——	53.73 ± 2.51	54.69 ± 2.30	52.78 ± 3.58
	Input concat. + S-DSAE	1000-50-20	80.33 ± 2.20	78.42 ± 3.27	82.19 ± 2.02
	S-DSAE + Output concat.	···-60	80.16 ± 0.80	75.86 ± 1.42	**84.37 ± 0.76**
	Multi-modal S-DSAE	···-8	**80.91 ± 1.53**	**79.07 ± 2.27**	82.70 ± 1.35

As we can see from the results, the adopted MM-S-DSAE has the best overall classification performance: it produces the highest ACC, SPE for AD vs. NC

[5] For "input concat. + S-DSAE" fusion strategy, we present the optimal number of hidden nodes for each of three hidden layer (bottom to up); for "S-DSAE + Output concat." and MM-S-DSAE fusion strategies, we only present the number of hidden nodes for the last concatenation or fusion layer, since the previous layers stay the same as in single modal stacked DSAE.

classification and the highest ACC, SEN for MCI vs. NC classification. While not surpassing the other two deep fusion strategies in all measures, the MM-S-DSAE does learn a much more compact high level feature representation than the other two deep fusion strategies, with better or comparable classification performance. Specifically, for "Input concatenation + Stacked DSAE" strategy, the optimal node size of the output layer is 10 in AD vs. NC classification, and 20 in MCI vs. NC classification; for "Stacked DSAE + Output concatenation" strategy, the optimal node size of the output concatenation layer is 70 in AD vs. NC classification, and 60 in MCI vs. NC classification; for MM-S-DSAE strategy, the optimal node size of the output fusion layer is 8 in both AD vs. NC and MCI vs. NC classifications. Compared to the original raw feature dimension (313), our MM-S-DSAE was able to achieve 97.5% feature dimension reduction.

4.4. Comparisons of TML-SVM with other classifiers

The last set of experiments seeks to test the effectiveness of the nonlinear feature transformation introduced by our proposed TML-SVM classifier in improving AD/MCI vs. NC classifications. We compare TML-SVM against two other classifiers without feature transformation: softmax regression and traditional SVM. For all the three classifiers, the same MM-S-DSAE model is used to obtain the fused feature representations. It is worth noting that only the deep network in softmax regression model is fine-tuned. For SVM, the slackness coefficient C is selected from $\{2^{-5} \sim 2^{15}\}$. TML-SVM has three hyper-parameters to be tuned: the number of anchor points p and the tradeoff coefficients C_1 and C_2. For p, we empirically set it to 30% of the training samples; for C_1 and C_2, we select them from $\{2^{-5} \sim 2^{15}\}$ and $\{5^{-5} \sim 5^{25}\}$ respectively. We still adopt the same experimental setting and performance measures, and report the results averaged from 10 runs in Table 5.

As evident, our TML-SVM has the best classification performance with the highest ACC, SEN, SPE for both AD vs. NC and MCI vs. NC classifications. In particular, the improvements made by TML-SVM over the host classifier

Table 5: Comparisons of three different classifiers for AD vs. NC and MCI vs. NC classifications.

	AD versus NC(%)			**MCI versus NC**(%)		
Classifier	**ACC**(%)	**SEN**(%)	**SPE**(%)	**ACC**(%)	**SEN**(%)	**SPE**(%)
Softmax	88.73 ± 1.04	84.86 ± 2.08	91.69 ± 1.68	80.91 ± 1.53	79.07 ± 2.27	82.70 ± 1.35
SVM	89.50 ± 0.86	87.16 ± 1.97	91.27 ± 1.02	80.52 ± 1.24	80.13 ± 2.58	80.93 ± 1.71
TML-SVM	**91.95 ± 1.00**	**89.49 ± 2.37**	**93.82 ± 1.63**	**83.72 ± 1.16**	**84.74 ± 2.34**	**82.72 ± 1.19**

SVM are significant (for AD vs. NC, p-values < 0.03; for MCI vs. NC, p-values < 0.02), which means adding the nonlinear feature transformation is effective in making the mapped data points more linearly separable. Also, we note that the deep neural networks used in SVM and TML-SVM are not fine-tuned as in softmax regression model, thus we believe the performance of our TML-SVM can be further improved if fine-tuning is utilized.

4.5. Comparisons with state-of-the-art AD staging methods

Numerous solutions [27, 28, 29, 25, 30, 31, 32] have been proposed in the literature for AD/MCI patient classification. Some very recent works [27, 30] reported rather high accuracies through the applications of multi-modality information integration (mainly MRIs and PETs) and sophisticated multi-classifier decision fusion schemes. Analysis of the solutions striving to address the same problem is crucial to advance the developments of highly effective methods. However, direct comparisons of the published neuroimaging algorithms are often not feasible, unless common subjects, datasets and modalities are employed, as in the evaluation project conducted by Cuingnet *et al.* [28]. When different datasets and experimental setups are utilized, which is common for many neuroimage studies, higher accuracy or better results over a competing solution ought to be interpreted as indirect evidence of the model efficacy, rather than the proof of superiority for head-to-head competitions.

We conduct the first set of comparisons with the solutions that are very close to our model in nature. Four recently published works are chosen: 1) voxel-wise GM densities based method by Kloppel *et al.* [21] which obtained the best performance among the ten methods evaluated in [28]; 2) 93-region

GM densities method by Zhang *et al.* [29], 3) the single classifier results using patch-wise GM, as presented in Liu *et al.* [25], and 4) a longitudinal work by McEvoy *et al.* [34], which uses the quadratic discriminant analyses (QDAs) as the classifier with ROI features extracted from the baseline and one-year follow-up information. Unlike the "DM" features in our work, the subtraction-based atrophy calculation in [34] is not dynamic. Similar to our method, these four solutions all use MR images as the sole information source and rely on single classifiers for classification. The comparison results are shown in Table 6.

Table 6: Comparisons of our proposed method with other existing methods for AD vs. NC and MCI vs. NC classifications within the same category.

Method	Study	Feature	Classifier	AD versus NC			MCI versus NC		
	Size			ACC(%)	SEN(%)	SPE(%)	ACC(%)	SEN(%)	SPE(%)
Cuingnet *et al.*[28]	475	Voxel-wise GM	SVM	88.6	81.0	**95.0**	81.2	73.0	**85.0**
Zhang *et al.*[29]	202	93 ROI GMs	SVM	86.2	86.0	86.3	72.0	78.5	59.6
Liu *et al.*[25]	652	Patch-wise GM	SVM	86.4	83.9	88.6	79.4	79.2	79.5
McEvoy *et al.* [34]	684	8 ROI volumes	QDAs	90.8	**91.3**	90.5	—	—	—
Proposed	338	Fused G/D/A	TML-SVM	**91.95**	89.49	93.82	**83.72**	**84.74**	82.72

From Table 6, we make the following observations. Our proposed model performs better than the competing methods in terms of classification accuracy in AD vs. NC classification, and accuracy and sensitivity in MCI vs. NC classification. Although the results for specificity reported in [28] are slightly higher than ours, it is at the expense of sacrificing sensitivity, leading to a worse accuracy. Researchers in [34] reported the highest sensitivity for AD vs. NC classification, but their accuracy and specificity are relatively lower than those produced in our method. In addition, compared to those three methods [28, 29, 25] that only use cross-sectional information at the baseline visits, our method achieves consistently better accuracy and sensitivity in both AD vs. NC and MCI vs. NC classifications. It is worth noting that high sensitivity may be advantageous for confident AD diagnosis at early stage, which is potentially useful in clinical practice.

In addition, we compare our model with six works that have reported very high, if not the highest, classification rates for AD/MCI vs. NC. The results are shown in Table 7. Five of them use cross-sectional information. The works of Suk *et al.* [27] and Liu *et al.* [30] are built on deep neural networks, and their high performance should not be a surprise as they both utilize PET as an additional feature source. The single-classifier version of Liu *et al.* [25] shown in Table 6 is outperformed by our model, but their multi-SVM version, through sophisticated multi-classifier decision fusion schemes, produces significantly improved results. Liu *et al.* [31, 32] use multiple templates and combine the outputs from multiple SVMs to achieve impressively high accuracies. Li *et al.* [33] use multi-year longitudinal information, including scans from 36-month visits, in their solution. As AD patients' late scans are commonly more revealing than those at baseline, very accurate diagnosis (96.1%) becomes possible.

While our model is single-classifier based, it achieves comparable performance with some of the aforementioned multi-classifier solutions. Upgrading our TPS-SVM with multi-kernel or multiple SVMs, or applying metric learning to the solutions in Table 7, could both potentially lead to performance improvements for the respective models. Structure MRIs are the sole information source of our current solution, therefore it can be expected that the performance of our model can be further improved if additional modalities, e.g., PET, functional MRI or diffusion tensor imaging (DTI), are integrated as inputs. All in all, we believe our pipeline achieves rather high accuracy in AD/MCI vs. NC classification with simple setups and limited information sources (structural MRIs alone), and lays a solid foundation for further integration and generalization.

Table 7: Comparisons of the proposed TML-SVM with state-of-the-art methods for AD vs. NC and MCI vs. NC classifications.

Method	Study	Modality	Classifier	AD versus NC			MCI versus NC		
	Size			ACC(%)	SEN(%)	SPE(%)	ACC(%)	SEN(%)	SPE(%)
Liu *et al.*[25]	652	MRI	Hierarchical fusion	92.0	90.9	93.0	85.3	82.3	88.2
Suk *et al.*[27]	398	MRI + PET	Deep Boltzmann machine	95.4	94.7	**95.2**	**85.7**	**95.4**	65.9
Liu *et al.*[30]	331	MRI + PET	Stacked parse auto-encoder	91.4	92.3	90.4	82.1	60.0	**92.3**
Liu *et al.*[31]	331	MRI	SVM ensemble	92.51	92.89	88.3	—	—	—
Liu *et al.*[32]	331	MRI	SVM ensemble	93.06	**94.85**	90.49	—	—	—
Li *et al.*[33]	152	MRI	SVM	**96.1**	—	—	—	—	—
Proposed	338	MRI	TML-SVM	91.95	89.49	93.82	83.72	84.74	82.72

5. Discussions and Conclusions

This study is designed with two major goals: 1) to develop a nonlinear metric learning solution and to explore if AD/MCI diagnosis can benefit from it; and 2) exploring how cross-sectional (baseline) and longitudinal (atrophy rates) information can be effectively integrated.

Metric learning has been an active research area in machine learning for more than a decade, but its ability to improve supervised and semi-supervised classification has not been fully recognized in neuroimaging community. Our TML-SVM model learns a globally smooth deformation for the input space, and it is the first work that utilizes nonlinear dense transformations, or spatially varying deformation models in metric learning. Using the ADNI dataset, we evaluated the effectiveness of our TML-SVM mode in improving AD/MCI diagnosis, and we hope a take-home message will be delivered to the neuroimaging community: metric learning does help.

Our proposed MM-S-DASE model is a deep learning solution to extract latent, high-level integrated feature representation from three raw features obtained through conventional feature engineering pipeline often used for statistical analysis and segmentation. Although deep learning methods are proven for automatically extracting meaningful representation from raw images, transplanting them to neuroimaging applications is often not trivial. Firstly, neuroimages are commonly high-resolution 3D images, tens or hundreds times larger than photographic 2D images. This creates much higher dimensional inputs if the volumetric images are used directly. Secondly, deep learning works best with large numbers of training samples, which are typically unavailable for individual clinical trials and human subject studies. These two factors significantly restrict the power of deep learning in neuroimaging applications. Patch features and patch-based learning, in our opinion, provide a remedy for both issues, and therefore can help bridge the research gap between computer vision and neuroimage analysis. Further efforts to explore patch-based solutions in neuroimaging appear warranted.

As multimodality images can provide complementary information in disease diagnoses, combining different modalities will likely lead to more accurate decision boundaries. The high accuracies reported in [27, 23] support this notion. Vast amounts of imaging and other data are collected on patients every day as part of standard medical care, yet virtually none of it is aggregated, processed and extracted using deep learning and related methods to support physician decision making at the present time. The exciting long term potential for this role should be clear just from the example of research we have presented here. But research requires focus. In the future work, we will explore features from other data modalities, including PET, fMRI, DTI, and genetic data. Enhancing our TML-SVM with multi-kernelization, as well as exploring other geometric models than TPS, are among the directions of our ongoing efforts.

6. Acknowledgments

This study was financially supported by grants by Stocker Endowment, Moores Alzheimer Research Endowment, Sanders-Brown Center on Aging and University of Kentucky College of Medicine.

Data collection and sharing for this project was funded by the Alzheimer's Disease Neuroimaging Initiative (ADNI) (National Institutes of Health Grant U01 AG024904) and DOD ADNI (Department of Defense award number W81XWH-12-2-0012). ADNI is funded by the National Institute on Aging, the National Institute of Biomedical Imaging and Bioengineering, and through generous contributions from the following: AbbVie, Alzheimers Association; Alzheimers Drug Discovery Foundation; Araclon Biotech; BioClinica, Inc.; Biogen; Bristol-Myers Squibb Company; CereSpir, Inc.; Eisai Inc.; Elan Pharmaceuticals, Inc.; Eli Lilly and Company; EuroImmun; F. Hoffmann-La Roche Ltd and its affiliated company Genentech, Inc.; Fujirebio; GE Healthcare; IXICO Ltd.; Janssen Alzheimer Immunotherapy Research & Development, LLC.; Johnson & Johnson Pharmaceutical Research & Development LLC.; Lumosity; Lundbeck; Merck & Co., Inc.; Meso Scale Diagnostics, LLC.; NeuroRx Research; Neurotrack Technologies; Novartis Pharmaceuticals Corporation; Pfizer Inc.; Piramal Imaging; Servier; Takeda Pharmaceutical Company; and Transition Therapeutics. The Canadian Institutes of Health Research is providing funds to support ADNI clinical sites in Canada. Private sector contributions are facilitated by the Foundation for the National Institutes of Health (www.fnih.org). The grantee organization is the Northern California Institute for Research and Education, and the study is coordinated by the Alzheimer's Disease Cooperative Study at the University of California, San Diego. ADNI data are disseminated by the Laboratory for Neuro Imaging at the University of Southern California.

7. Appendix: Names of the 113 anatomical structures in Aseg features

The *Aseg* feature set in this study consists of the volumes of 113 cortical and subcortical brain structures extracted from the *FreeSurfer Cross-Sectional Processing aparc+aseg segmentation* files, available under ADNI. These structures were segmented from the subjects' T1-weighted MRI scans. All features have been normalized by the corresponding whole brain volumes. The list of the structure names is provided as follows. **Aseg** list contains subcortical structures, and **Aparc** is for cortical structures.

Aseg structures Left-Lateral-Ventricle, Left-Inf-Lat-Vent, Left-Cerebellum-White-Matter, Left-Cerebellum-Cortex, Left-Thalamus-Proper, Left-Caudate, Left-Putamen, Left-Pallidum, 3rd-Ventricle, 4th-Ventricle, Brain-Stem, Left-Hippocampus, Left-Amygdala, CSF, Left-Accumbens-area, Left-VentralDC, Left-vessel, Left-choroid-plexus, Right-Lateral-Ventricle, Right-Inf-Lat-Vent, Right-Cerebellum-White-Matter, Right-Cerebellum-Cortex, Right-Thalamus-Proper, Right-Caudate, Right-Putamen, Right-Pallidum, Right-Hippocampus, Right-Amygdala, Right-Accumbens-area, Right-VentralDC, Right-vessel, Right-choroid-plexus, 5th-Ventricle, WM-hypointensities, Left-WM-hypointensities, Right-WM-hypointensities, non-WM-hypointensities, Left-non-WM-hypointensities, Right-non-WM-hypointensities, Optic-Chiasm, CC-Posterior, CC-Mid-Posterior, CC-Central, CC-Mid-Anterior, CC-Anterior.

Aparc structures ctx-lh-bankssts, ctx-lh-caudalanteriorcingulate, ctx-lh-caudalmiddlefrontal, ctx-lh-cuneus, ctx-lh-entorhinal, ctx-lh-fusiform, ctx-lh-inferiorparietal, ctx-lh-inferiortemporal, ctx-lh-isthmuscingulate, ctx-lh-lateraloccipital, ctx-lh-lateralorbitofrontal, ctx-lh-lingual, ctx-lh-medialorbitofrontal, ctx-lh-middletemporal, ctx-lh-parahippocampal, ctx-lh-paracentral, ctx-lh-parsopercularis, ctx-lh-parsorbitalis, ctx-lh-parstriangularis, ctx-lh-pericalcarine, ctx-lh-postcentral, ctx-lh-posteriorcingulate, ctx-lh-precentral, ctx-lh-precuneus, ctx-lh-rostralanteriorcingulate, ctx-lh-rostralmiddlefrontal, ctx-lh-superiorfrontal, ctx-lh-superiorparietal, ctx-lh-superiortemporal, ctx-lh-supramarginal, ctx-lh-frontalpole, ctx-lh-temporalpole, ctx-lh-transversetemporal, ctx-lh-insula, ctx-rh-bankssts, ctx-rh-caudalanteriorcingulate, ctx-rh-caudalmiddlefrontal, ctx-rh-cuneus, ctx-rh-entorhinal, ctx-rh-fusiform, ctx-rh-inferiorparietal, ctx-rh-inferiortemporal, ctx-rh-isthmuscingulate, ctx-rh-lateraloccipital, ctx-rh-lateralorbitofrontal, ctx-rh-lingual, ctx-rh-medialorbitofrontal, ctx-rh-middletemporal, ctx-rh-parahippocampal, ctx-rh-paracentral, ctx-rh-parsopercularis, ctx-rh-parsorbitalis, ctx-rh-parstriangularis, ctx-rh-pericalcarine, ctx-rh-postcentral, ctx-rh-posteriorcingulate, ctx-rh-precentral, ctx-rh-precuneus, ctx-rh-rostralanteriorcingulate, ctx-rh-rostralmiddlefrontal, ctx-rh-superiorfrontal, ctx-rh-superiorparietal, ctx-rh-superiortemporal, ctx-rh-supramarginal, ctx-rh-frontalpole, ctx-rh-temporalpole, ctx-rh-transversetemporal, ctx-rh-insula.

8. References

[1] A. Alzheimers, 2015 Alzheimer's disease facts and figures., Alzheimer's & dementia: the journal of the Alzheimer's Association 11 (3) (2015) 332.

[2] A. J. Mitchell, M. Shiri-Feshki, Rate of progression of mild cognitive impairment to dementia–meta-analysis of 41 robust inception cohort studies, Acta Psychiatrica Scandinavica 119 (4) (2009) 252–265.

[3] I. A. van Rossum, S. J. Vos, L. Burns, D. L. Knol, P. Scheltens, H. Soininen, L.-O. Wahlund, H. Hampel, M. Tsolaki, L. Minthon, et al., Injury markers predict time to dementia in subjects with MCI and amyloid pathology, Neurology 79 (17) (2012) 1809–1816.

[4] C. R. Jack, et al., The Alzheimer's disease neuroimaging initiative (ADNI): MRI methods, Journal of Magnetic Resonance Imaging 27 (4) (2008) 685–691.

[5] A. Bellet, A. Habrard, M. Sebban, A survey on metric learning for feature vectors and structured data, arXiv preprint arXiv:1306.6709.

[6] L. Yang, R. Jin, Distance metric learning: A comprehensive survey, Michigan State Universiy 2 (2006) 78.

[7] E. P. Xing, A. Y. Ng, M. I. Jordan, S. Russell, Distance metric learning with application to clustering with side-information, Advances in neural information processing systems 15 (2003) 505–512.

[8] J. Goldberger, G. E. Hinton, S. T. Roweis, R. Salakhutdinov, Neighbourhood components analysis, Advances in neural information processing systems (2004) 513–520.

[9] M. Schultz, T. Joachims, Learning a distance metric from relative comparisons, Advances in neural information processing systems (2004) 41.

[10] J. V. Davis, B. Kulis, P. Jain, S. Sra, I. S. Dhillon, Information-theoretic metric learning, in: Proceedings of the 24th international conference on Machine learning, ACM, 2007, pp. 209–216.

[11] K. Q. Weinberger, J. Blitzer, L. K. Saul, Distance metric learning for large margin nearest neighbor classification, Advances in Neural Information Processing Systems (2005) 1473–1480.

[12] A. Globerson, S. Roweis, Metric learning by collapsing classes, Advances in neural information processing systems (2005) 451–458.

[13] L. Torresani, K.-c. Lee, Large margin component analysis, Advances in neural information processing systems 19 (2007) 1385.

[14] J. T. Kwok, I. W. Tsang, Learning with idealized kernels, Proceedings of the Twentieth International Conference on Machine Learning (ICML-03) (2003) 400–407.

[15] R. Chatpatanasiri, T. Korsrilabutr, P. Tangchanachaianan, B. Kijsirikul, A new kernelization framework for Mahalanobis distance learning algorithms, Neurocomputing 73 (10) (2010) 1570–1579.

[16] K. Q. Weinberger, L. K. Saul, Distance metric learning for large margin nearest neighbor classification, The Journal of Machine Learning Research 10 (2009) 207–244.

[17] Y. Hong, Q. Li, J. Jiang, Z. Tu, Learning a mixture of sparse distance metrics for classification and dimensionality reduction, in: 2011 International Conference on Computer Vision, IEEE, 2011, pp. 906–913.

[18] D. Ramanan, S. Baker, Local distance functions: A taxonomy, new algorithms, and an evaluation, IEEE Trans. Pattern Anal. Mach. Intell. 33 (4) (2011) 794–806.

[19] Y.-K. Noh, B.-T. Zhang, D. D. Lee, Generative local metric learning for nearest neighbor classification, in: Advances in Neural Information Processing Systems, 2010, pp. 1822–1830.

[20] J. Wang, A. Kalousis, A. Woznica, Parametric local metric learning for nearest neighbor classification, in: Advances in Neural Information Processing Systems, 2012, pp. 1601–1609.

[21] S. Klöppel, et al., Automatic classification of MR scans in Alzheimer's disease, Brain 131 (3) (2008) 681–689.

[22] M. Chupin, A. Hammers, R. S. Liu, O. Colliot, J. Burdett, E. Bardinet, J. S. Duncan, L. Garnero, L. Lemieux, Automatic segmentation of the

hippocampus and the amygdala driven by hybrid constraints: method and validation, Neuroimage 46 (3) (2009) 749–761.

[23] H.-I. Suk, S.-W. Lee, D. Shen, A. D. N. Initiative, et al., Latent feature representation with stacked auto-encoder for AD/MCI diagnosis, Brain Structure and Function 220 (2) (2015) 841–859.

[24] Y. Fan, D. Shen, R. C. Gur, R. E. Gur, C. Davatzikos, Compare: classification of morphological patterns using adaptive regional elements, IEEE transactions on medical imaging 26 (1) (2007) 93–105.

[25] M. Liu, D. Zhang, D. Shen, Hierarchical fusion of features and classifier decisions for Alzheimer's disease diagnosis, Human brain mapping 35 (4) (2014) 1305–1319.

[26] G. Wu, M. Kim, G. Sanroma, Q. Wang, B. C. Munsell, D. Shen, A. D. N. Initiative, et al., Hierarchical multi-atlas label fusion with multi-scale feature representation and label-specific patch partition, NeuroImage 106 (2015) 34–46.

[27] H.-I. Suk, S.-W. Lee, D. Shen, A. D. N. Initiative, et al., Hierarchical feature representation and multimodal fusion with deep learning for AD/MCI diagnosis, NeuroImage 101 (2014) 569 – 582.

[28] R. Cuingnet, E. Gerardin, J. Tessieras, G. Auzias, S. Lehéricy, M.-O. Habert, M. Chupin, H. Benali, O. Colliot, A. D. N. Initiative, et al., Automatic classification of patients with Alzheimer's disease from structural MRI: a comparison of ten methods using the ADNI database, neuroimage 56 (2) (2011) 766–781.

[29] D. Zhang, Y. Wang, L. Zhou, H. Yuan, D. Shen, A. D. N. Initiative, et al., Multimodal classification of Alzheimer's disease and mild cognitive impairment, Neuroimage 55 (3) (2011) 856–867.

[30] S. Liu, S. Liu, W. Cai, H. Che, S. Pujol, R. Kikinis, D. Feng, M. J. Fulham, et al., Multimodal Neuroimaging Feature Learning for Multiclass Diagno-

sis of Alzheimer's Disease, IEEE Transactions on Biomedical Engineering 62 (4) (2015) 1132–1140.

[31] M. Liu, D. Zhang, D. Shen, View-centralized multi-atlas classification for Alzheimer's disease diagnosis, Human brain mapping 36 (5) (2015) 1847–1865.

[32] M. Liu, D. Zhang, D. Shen, Relationship induced multi-template learning for diagnosis of Alzheimers disease and mild cognitive impairment, IEEE transactions on medical imaging 35 (6) (2016) 1463–1474.

[33] Y. Li, Y. Wang, G. Wu, F. Shi, L. Zhou, W. Lin, D. Shen, Alzheimer's Disease Neuroimaging Initiative, et al., Discriminant analysis of longitudinal cortical thickness changes in Alzheimer's disease using dynamic and network features, Neurobiology of aging 33 (2) (2012) 427–e15.

[34] L. K. McEvoy, D. Holland, D. J. Hagler Jr, C. Fennema-Notestine, J. B. Brewer, A. M. Dale, Mild cognitive impairment: baseline and longitudinal structural MR imaging measures improve predictive prognosis, Radiology 259 (3) (2011) 834–843.

[35] B. jie, M. Liu, J. Liu, D. Zhang, D. Shen, Temporally-constrained group sparse learning for longitudinal data analysis in Alzheimer's disease, IEEE Transactions on Biomedical Engineering PP (99) (2016) 1–1. doi:10.1109/TBME.2016.2553663.

[36] H.-I. Suk, S.-W. Lee, D. Shen, A hybrid of deep network and hidden markov model for MCI identification with resting-state fMRI, in: International Conference on Medical Image Computing and Computer-Assisted Intervention, Springer, 2015, pp. 573–580.

[37] Z. Xu, K. Q. Weinberger, O. Chapelle, Distance metric learning for kernel machines, arXiv preprint arXiv:1208.3422.

[38] X. Zhu, P. Gong, Z. Zhao, C. Zhang, Learning similarity metric with SVM, in: The 2012 International Joint Conference on Neural Networks (IJCNN), IEEE, 2012, pp. 1–8.

[39] G. Wahba, Spline models for observational data, Vol. 59, Siam, 1990.

[40] J. Duchon, Splines minimizing rotation-invariant semi-norms in Sobolev spaces, in: Constructive theory of functions of several variables, Springer, 1977, pp. 85–100.

[41] H. Chui, A. Rangarajan, A new point matching algorithm for non-rigid registration, Computer Vision and Image Understanding 89 (2) (2003) 114–141.

[42] L. Kaufman, P. Rousseeuw, Clustering by means of medoids, North-Holland, 1987.

[43] H.-S. Park, C.-H. Jun, A simple and fast algorithm for k-medoids clustering, Expert Systems with Applications 36 (2) (2009) 3336–3341.

[44] H. Do, A. Kalousis, M. Hilario, Feature weighting using margin and radius based error bound optimization in svms, in: Joint European Conference on Machine Learning and Knowledge Discovery in Databases, Springer, 2009, pp. 315–329.

[45] A. Mechelli, C. J. Price, K. J. Friston, J. Ashburner, Voxel-based morphometry of the human brain: methods and applications, Current Medical Imaging Reviews 1 (2) (2005) 105–113.

[46] B. B. Avants, N. Tustison, G. Song, Advanced normalization tools (ANTS), Insight J (2009) 1–35.

[47] B. Fischl, Freesurfer, Neuroimage 62 (2) (2012) 774–781.

[48] B. Fischl, D. H. Salat, E. Busa, M. Albert, M. Dieterich, C. Haselgrove, A. Van Der Kouwe, R. Killiany, D. Kennedy, S. Klaveness, et al., Whole

brain segmentation: automated labeling of neuroanatomical structures in the human brain, Neuron 33 (3) (2002) 341–355.

[49] A. Gupta, M. Ayhan, A. Maida, Natural image bases to represent neuroimaging data, in: Proceedings of the 30th International Conference on Machine Learning (ICML-13), Vol. 28, JMLR Workshop and Conference Proceedings, 2013, pp. 987–994.
URL http://jmlr.org/proceedings/papers/v28/gupta13b.pdf

[50] P. Vincent, H. Larochelle, Y. Bengio, P.-A. Manzagol, Extracting and composing robust features with denoising autoencoders, in: Proceedings of the 25th international conference on Machine learning, ACM, 2008, pp. 1096–1103.

[51] Y. Bengio, Learning deep architectures for AI, Foundations and trends® in Machine Learning 2 (1) (2009) 1–127.